IOP Publishing Journal of Physics: Condensed Matter
J. Phys.: Condens. Matter **32** (2020) 205301 (13pp) https://doi.org/10.1088/1361-648X/ab6b8d

Mechanical properties of CNT-reinforced Ni_3Al composites: the role of chirality, temperature, and volume fraction

Zhaowei Wang[1], Fan Yang[1], Jing Shang[1,2], Ning Wei[3], Liangzhi Kou[2] and Chun Li[1,4,5]

[1] School of Mechanics, Civil Engineering and Architecture, Northwestern Polytechnical University, Xi'an 710129, People's Republic of China
[2] School of Chemistry, Physics and Mechanical Engineering Faculty, Queensland University of Technology, Garden Point Campus, Brisbane, QLD 4001, Australia
[3] Jiangsu Key Laboratory of Advanced Food Manufacturing Equipment and Technology, Jiangnan University, Wuxi 214122, People's Republic of China
[4] Department of Mechanical Engineering, University of Manitoba, Winnipeg MB R3T 5V6, Canada

E-mail: lichun@nwpu.edu.cn

Received 15 October 2019, revised 13 December 2019
Accepted for publication 14 January 2020
Published 18 February 2020

Abstract

Ni_3Al is an extremely significant reinforcing phase in nickel-based single crystal superalloys. As an alternative strengthening method to improve its mechanical properties, carbon nanotube (CNT)-reinforced Ni_3Al composites have recently been synthesized in experiments. Here, in order to explore the corresponding influence factors and the underlying mechanism, tensile and compressive mechanical properties of CNT-Ni_3Al composites are systematically investigated by using molecular dynamics simulations. It is shown that the dispersion of a minor fraction of a CNT into Ni_3Al matrix leads to a sufficient enhancement in the stiffness of CNT-Ni_3Al composites compared with the pure Ni_3Al. It is demonstrated that CNT reinforcement takes effect in the elastic stage under compression while it works continuously during tension. Compared with armchair CNTs, zigzag CNTs are predicted to provide more strength for raising the elastic modulus while armchair CNTs can provide superior elongation. Particularly, CNTs are found to hinder the generation of slip bands under tensile loading owing to the robust interfacial interactions. Furthermore, quantitative analysis reveals that the impact of volume fraction of CNT is much more significant than the size effect. The role of chirality, temperature and volume fraction of CNT obtained in the present work could provide beneficial references for subsequent theoretical and experimental investigations, and shed some light on the design of CNT-reinforced composites in nanoscale engineering.

Keywords: CNT-Ni_3Al composite, mechanical properties, molecular dynamics

S Supplementary material for this article is available online

(Some figures may appear in colour only in the online journal)

1. Introduction

Nickel based single crystal superalloy has been extensively facilitated in high-temperature applications, especially as structure materials in aircraft turbine blades. These intermetallic materials possess many excellent properties, including low density, high melting point, good oxidation and corrosion resistance [1, 2]. Furthermore, the γ' phase: Ni_3Al matrix which takes around 70% volume fraction is an important strengthening phase. Ni_3Al is an intermetallic alloy with a

[5] Author to whom any correspondence should be addressed.

face-centered-cubic $L1_2$ structure. However, Ni_3Al is a type of brittle material, which limits its wider applications. Therefore, Ni_3Al has been investigated deeply among all aspects of its properties to improve its mechanical property like toughness and working ages under extreme working conditions [3, 4]. On the other hand, since the discovery of carbon nanotubes (CNTs) by Iijima [5], great efforts have been devoted to study these new-born materials as an effective reinforce element for composite for their unique mechanical properties containing low density, much higher Young's modulus, great tensile stress, and fracture strain [6, 7]. In the last decade, more attention has been paid on the simulation of CNT-polymer composites [8–10]. While in recent years, the mechanical properties of CNT-reinforced metal matrix (mainly Al, Cu, and Mg) composite (MMCs) and its potential applications have been widely investigated from both experimental and computational aspects [11–13].

As far as experiments are concerned, to achieve satisfactory and outstanding fabrication of CNT-reinforced MMCs, CNTs should disperse uniformly in metal matrix along a certain direction [14, 15]. Apart from that, some experimental studies have focused on how to strengthen the relative weak adhesion in the interface [16, 17]. Chen *et al* reported that the Ni–P coated carbon nanotubes (NiPCNTs) were dispersed into Nickel-based superalloy Inconel 718 (IN718) powder by ball milling and then tensile mechanical properties (yield strength, ultimate strength and ductility) of the as-deposited coatings were evaluated [18]. However, until now most experimental work still have been carried out to focus on achieving a homogenous dispersion of CNTs and its consecutive influences on mechanical properties of whole structure [19, 20]. Experimental studies mainly focus on fabrication technics and phenomenon from macro perspectives, while atomistic simulations can effectively predict the mechanical properties of nanoscale structures [21–24].

In numerical methods, molecular dynamics (MD) is regarded as the appropriate one to predict mechanical properties of nanoscale materials. Particularly MD simulations have advantages for tracking dynamic trajectories of the atoms. Among them, Silvestre *et al* analysed the mechanical properties of CNT-Al composites under compression [22]. It was concluded that in comparison with pure Al, the Young's modulus increased about 50%–100%. These increases were due to the inherent axial stiffness of the CNT and also to non-negligible interface slip stress values. Zhou *et al* simulated the mechanical properties of the Ni-coated or uncoated armchair single-wall CNT (SWCNT)/magnesium matrix composites under axial tension and the pullout behavior of the SWCNT from the Mg matrix with various Ni-coated thickness [23]. It indicated that surface Ni coating of SWCNTs can provide an effective channel for load transfer of the SWCNT and Mg matrix. Choi *et al* investigated the mechanical behavior of CNT-reinforced aluminum composite with various CNT diameters [24]. The overall mechanical properties, such as Young's modulus and toughness, increased considerably as the CNT reinforcement was increased. It was also observed the stress decreases were shown to be due to the combination of lattice structure change, dislocation, stacking faults, and micro-void nucleation. Xiang *et al* used periodic boundary conditions to model an Al matrix embedded with CNTs of different chiralities, lengths and diameters. They established that significant improvements on stiffness, strength and elasticity of the nanocomposite can be achieved by the inclusion of small volume fractions of CNTs [25].

As for Ni_3Al, various studies have focused on the mechanical properties of Ni_3Al material with respect to the doped alloying elements [26] or preset defects [27]. Recently, researchers have reported a successful fabrication of CNT-Ni_3Al composites using wet ball milling process technic [28]. However, the research on the mechanical properties of CNT-reinforced Ni_3Al, especially the corresponding influence factors and the underlying mechanism, is still limited nowadays. On the other hand, large amount of reports have confirmed that CNT is truly a promising reinforcing phase both experimentally and theoretically. So in this study, by using MD simulations, we want to explore whether CNT could bring distinct reinforcement effect by considering the influences of the chirality, temperature, and volume fraction of the inserted CNTs. The present work could provide comprehensive attention to the distinct behaviors of CNT-reinforced composites under tension and compression.

2. Computational methods

2.1. Simulation models

The initial unit cell of CNT-Ni_3Al composite adopted in the present simulations is shown in the figure 1. The Ni_3Al matrix is established in a square prism shape with crystal lattice constant of Ni_3Al $a = 3.57$ Å according to other experimental measuring and first-principle results [29, 30]. The dimensions of unit cell are $14a \times 14a \times 25a$ in x, y, z directions, respectively. The x, y, z axes are initially aligned with the Ni_3Al lattice orientations of [1 0 0], [0 1 0], and [0 0 1], respectively. To insert a CNT appropriately, a corresponding cylindrical hole along Ni_3Al matrix height should be wiped out at the centre so as to allow putting embedded CNTs according to their radii(eg.,(4,4) to (12,12), (10,0) to (18,0)). In present study, the radii are 2.757 Å, 4.125 Å, 5.513 Å, 6.892 Å, 8.204 Å for armchair CNTs and 3.975 Å, 4.775 Å, 5.570 Å, 6.366 Å, 7.162 Å for zigzag CNTs. In addition, a distance of 3 Å between C and Ni, Al atoms is ensured to guarantee precise interatomic interactions [31]. A pure Ni_3Al unit cell of the same geometry is calculated as a reference.

2.2. Simulation details

Before carrying out the tensile simulation, the unit cell is primarily minimized to a rather low-energy state through conjugate gradient energy minimization algorithm. After that, a further structure relaxation is conducted under the constant temperature of 300 K and constant pressure of 0 bar (NPT ensemble) through Nóse–Hoover thermostat and barostat with a timestep of 0.5 fs for 100 ps to eliminate internal residual stresses and stabilize the whole structure before following simulations.

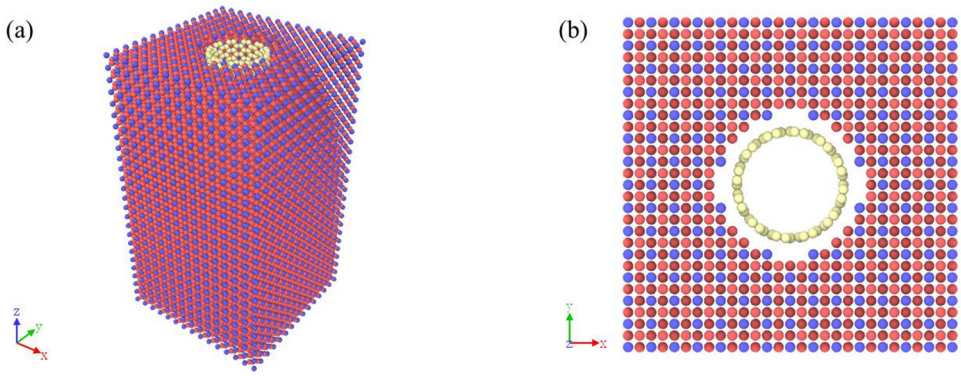

Figure 1. The (12,12) CNT-Ni_3Al composite model with (a) the side view (b) the top view. Red atoms represent Ni, blue atoms represent Al, white atoms represent C.

During the MD simulations, an engineering strain rate of $\pm 5 \times 10^{-4}$ ps^{-1} is applied along the z axis which is similar to typical strain rates used in other MD simulations [25, 32] until strain reaching 50% for 1000 ps with a timestep of 0.5 fs. The NVT and NPT ensembles are set during the simulation at 300 K under tensile and compressive conditions, respectively. Periodic boundary conditions are applied in all three dimensions in order to minimize the size effects induced by the limited size of simulation model. All MD simulations are performed using the large scale atomic/molecular massively parallel simulator (LAMMPS) code [33].

2.3. Potential functions

In general, the accuracy of a simulation relies on the choice of the potential functions for whether they can describe all atomic interactions comprehensively and exactly. For the CNT-Ni_3Al composite, the total energy of the system is

$$E_{\text{total}} = E_{\text{Ni}_3\text{Al}} + E_{\text{CNT}} + E_{\text{C–Ni}} + E_{\text{C–Al}}, \tag{1}$$

where $E_{\text{Ni}_3\text{Al}}$ is the total potential energy between Ni and Al atoms, E_{CNT} is the total potential energy between carbon atoms, and $E_{\text{C–Ni}}$ and $E_{\text{C–Al}}$ are the total potential energy between interfacial atoms at the CNT-Ni_3Al interface.

The embedded atom method (EAM) potential developed by Mishin *et al* [34] where the atomic potential energy consists of two parts is employed to simulate the atomic interactions of the Ni_3Al matrix as follows

$$E_i = F_\alpha\left(\sum_{j\neq i} \rho_\beta(r_{ij})\right) + \frac{1}{2}\sum_{j\neq i} \phi_{\alpha\beta}(r_{ij}), \tag{2}$$

where F is the embedding energy which is a function of the atomic electron density ρ, ϕ is a pair potential interaction, and α and β are the element types of atoms i and j, respectively. The multi-body nature of the EAM potential is a result of the embedding energy term. Both summations in the formula are over all neighbors j of atom i within the cutoff distance.

The adaptive intermolecular reactive empirical bond order (AIREBO) Potential is adopted to describe the C–C interaction within the CNT [35]. The AIREBO potential is taken since it has been proven to be accurate to describe the mechanical properties of CNT. The potential is composed of the reactive empirical bond order (REBO) potential, the Lennard-Jones (L-J) potential, and the torsional interaction potential are given as follows:

$$E = \frac{1}{2}\sum_i \sum_{j\neq i} [E_{ij}^{\text{REBO}} + E_{ij}^{\text{LJ}} + \sum_{k\neq i,j} \sum_{l\neq i,j,k} E_{kijl}^{\text{TORSION}}], \tag{3}$$

where the three terms on the right side describe the covalent bonding forces, intermolecular interaction, and the dihedral angle effect, respectively. The cutoff parameter of potential is referred from Choi *et al* [24] and the parameter of C–C interaction has been modified from 1.7 to 2.0 to better conform to experimental results.

Considering both accuracy and computational cost, for the interaction between CNT and Al, Ni atoms in Ni_3Al matrix, covalent and non-covalent interaction is taken into account. The L-J (12-6) potential offers a reasonable option [24], which is adopted as:

$$E = 4\varepsilon[(\frac{\sigma}{r})^{12} - (\frac{\sigma}{r})^{6}] \qquad r < r_c, \tag{4}$$

where ε is the depth of the potential well, σ is the distance where the interatomic potential is zero. Both these two parameters are determined by the mixture rules of Lorentz–Berthelot. The ε and σ are calculated as the geometric average of $\varepsilon_{12} = \sqrt{\varepsilon_{11}\varepsilon_{22}}$ and the arithmetic average of $\sigma_{12} = (\sigma_{11} + \sigma_{22})/2$, respectively. In this work, $\varepsilon_{13} = 0.024\,99$ eV and $\sigma_{13} = 2.85$ Å for Ni–C interaction are chosen from Huang *et al* [36, 37], and $\varepsilon_{23} = 0.034\,36$ eV and $\sigma_{23} = 3.01$ Å for Al–C interaction are adopted from Choi *et al* [24]. The numbers 1, 2, and 3 denote Ni, Al, and C atoms, respectively. The cutoff radius is set as 10 Å, which is larger than $3\sigma_{23}$ (9.03 Å), in order to avoid truncation errors.

The most challenging issue in the description of interactions between CNT and Ni atoms. Throughout previous MD simulation reports, many researchers adopt Brenner-type potential developed by Yasushi Shibuta *et al* [38], which has been proved to be the most accurate one to describe this covalent interactions between CNT and Ni atoms [21, 39, 40]. However, it is not available for everyone since it needs work to compound. So, to minimize the deviation of our research, we would like to utilize the relatively reliable L-J potential [23, 36, 37] and pairwise Morse potential [41, 42] to simulate

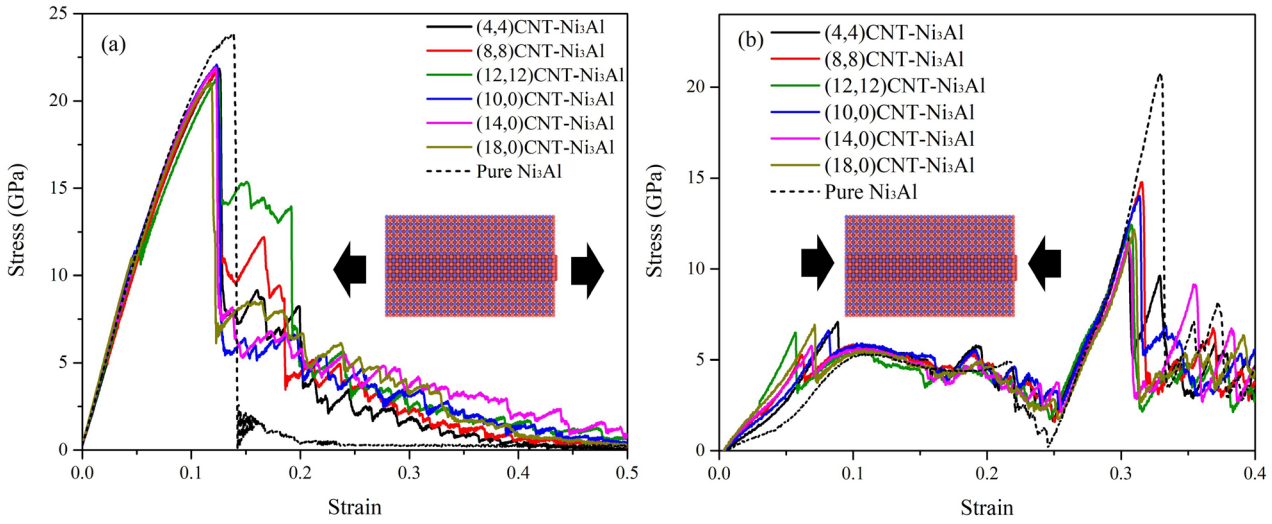

Figure 2. Stress–strain curves of CNT-reinforced Ni_3Al composites with different radii and chiralities under (a) tensile loading, (b) compressive loading.

Table 1. Mechanical properties of CNT-Ni_3Al composites with different sizes and chiralities under tension.

Composites	Young's modulus (GPa)	Fracture stress (GPa)	Fracture strain
(4,4)CNT-Ni_3Al	211.42	8.23	0.1993
(6,6)CNT-Ni_3Al	229.92	10.90	0.1875
(8,8)CNT-Ni_3Al	225.46	8.71	0.1853
(10,10)CNT-Ni_3Al	221.65	13.10	0.1813
(12,12)CNT-Ni_3Al	219.44	13.92	0.1920
(10,0)CNT-Ni_3Al	236.87	14.99	0.1263
(12,0)CNT-Ni_3Al	229.73	13.15	0.1258
(14,0)CNT-Ni_3Al	236.94	12.45	0.1239
(16,0)CNT-Ni_3Al	232.23	13.70	0.1235
(18,0)CNT-Ni_3Al	243.21	12.18	0.1220
Pure Ni_3Al	218.17 (exp: 224.5)	16.69	0.1408

the C–Ni covalent interactions. Among many reports simulating with morse potential, huge differences can be found from each other. In this paper, the parameters $D_0 = 0.433$ eV, $\alpha = 3.244$ 1/Å, and $r_0 = 2.316$ Å are adopted from Katin's work [42]. Results of both potentials show minor difference (results of Morse potential is given in supporting information (stacks.iop.org/JPhysCM/32/205301/mmedia)), therefore, we believe the use of a Lennard-Jones potential is still reasonable as our focus is on the effects of CNT's geometric structure in strengthening the Ni_3Al matrix.

3. Results

3.1. Mechanical properties of CNT-reinforced Ni_3Al *composites*

The calculated stress–strain curves for pure Ni_3Al and CNTs-reinforced Ni_3Al composites with various CNT radii and chiralities under tensile loadings are shown in figure 2(a). It can be observed that in the small strain regime ($0 \leqslant \varepsilon \leqslant 0.07$) the relations between stresses and strains are almost linear for all cases, which denote the elastic deformation stage. The elastic moduli for all cases are obtained by calculating the slope ratios of stress–strain curves around zero ($0 \leqslant \varepsilon \leqslant 0.01$ for both loadings). The calculated Young's moduli of the studied CNT-Ni_3Al systems are listed in table 1. Compared with the value of pure Ni_3Al which is 218.17 GPa (in agreement with experiment: 224.5 GPa [43], DFT: 225.3 GPa [44], and MD: 224.2 GPa [45]), the elastic property of CNT-Ni_3Al composites are especially impacted by zigzag CNTs, showing a slightly larger increment (between 5.3% and 11.5%) while the values stay almost the same for armchair CNT-reinforced structures (between −3.1% and 5.4%). Further simulations have been done to find the ultra-large CNTs' performance ((16,16) and (20,20)) in composites, but no remarkable reinforcement effect has been found (the obtained elastic moduli are 219.45 GPa and 217.55 GPa, respectively). Meanwhile, large radius would exceed the size of matrix and become difficult to judge its reinforcement effect. With reference of previous reports [46–48], the minor improvement can still be found for larger radius but the trend is slowing down. Hence, it is believed the larger size CNT has fewer meanings for improving the elastic properties of the composites. On the other hand, figure 2(b) depicts the stress–strain curves under compression and the calculated Young's moduli are enhanced considerably by both armchair (between 25.7% and 99.6%) and zigzag (between

Table 2. Mechanical properties of various CNT-Ni_3Al composites under compression.

Composites	Young's modulus (GPa)	Yield stress (GPa)	Yield strain
(4,4)CNT-Ni_3Al	57.39	−7.09	−0.0886
(6,6)CNT-Ni_3Al	67.58	−6.33	−0.0739
(8,8)CNT-Ni_3Al	77.45	−5.29	−0.0619
(10,10)CNT-Ni_3Al	88.33	−4.68	−0.0575
(12,12)CNT-Ni_3Al	91.14	−6.53	−0.0568
(10,0)CNT-Ni_3Al	68.96	−6.61	−0.0814
(12,0)CNT-Ni_3Al	73.69	−6.45	−0.0568
(14,0)CNT-Ni_3Al	80.56	−5.74	−0.0689
(16,0)CNT-Ni_3Al	84.18	−4.84	−0.0594
(18,0)CNT-Ni_3Al	92.41	−6.90	−0.0714
Pure Ni_3Al	45.67	−5.21	−0.125

Table 3. Overall Young's modulus calculated from the rule of mixtures.

	Young's modulus (GPa)		Volume fraction (%)		Young's modulus (GPa)
Composites	Y_{CNT}	Y_{Ni_3Al}	V_{CNT}	V_{Ni_3Al}	$Y_{CNT\text{-}Ni_3Al}$
(4,4)CNT-Ni_3Al	846.93	191.87	2.48	97.52	208.12
(6,6)CNT-Ni_3Al	815.22	200.92	3.80	96.20	224.26
(8,8)CNT-Ni_3Al	848.94	185.90	5.24	94.76	220.64
(10,10)CNT-Ni_3Al	841.58	171.63	6.79	93.21	217.12
(12,12)CNT-Ni_3Al	878.74	159.08	8.41	91.59	219.60
(10,0)CNT-Ni_3Al	930.74	204.61	3.65	96.35	231.11
(12,0)CNT-Ni_3Al	962.56	190.81	4.46	95.54	225.23
(14,0)CNT-Ni_3Al	948.84	192.69	5.35	94.65	233.14
(16,0)CNT-Ni_3Al	939.65	178.18	6.24	93.76	225.69
(18,0)CNT-Ni_3Al	912.25	186.24	7.93	92.07	243.81

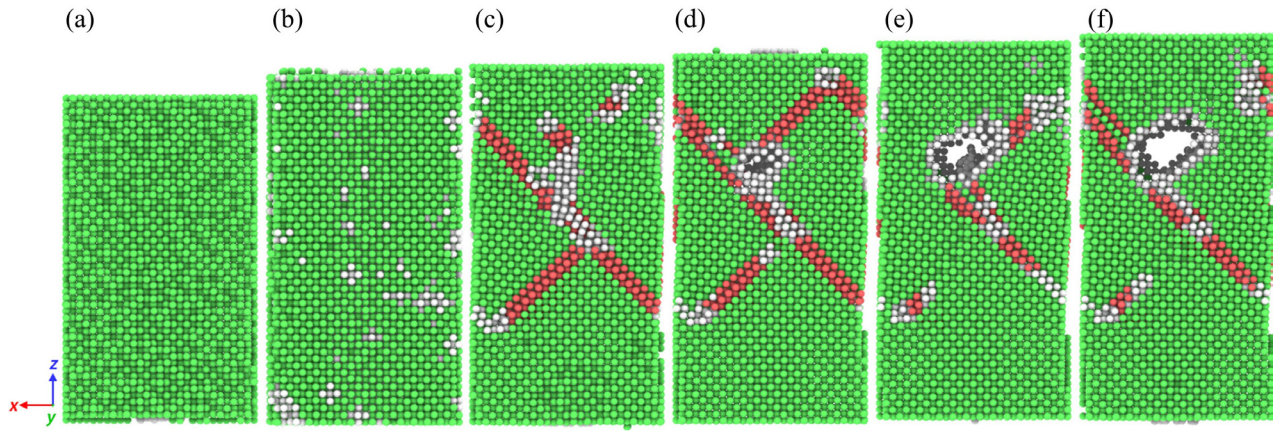

Figure 3. Snapshots of different lattice structures of (8,8) CNT-reinforced Ni_3Al at various strains: (a) 0.01, (b) 0.1, (c) 0.13, (d) 0.16, (e) 0.185 75, (f) 0.21.

51.0% and 102.3%) CNTs compared with 45.67 GPa (MD: 80 GPa [49]) of pure Ni_3Al (see table 2). From comparing the increments of Young's moduli under two deformation modes, it can be easy to find that tension brings weak influence. The poorer stretching properties should be led by both weaker armchair CNTs and cylinder void defects, which can be seen in table 3 with relatively lower elastic moduli of armchair CNTs and Ni_3Al phase.

Taking (8,8) CNT-Ni_3Al under tension as an example, in the region of $0.075 \leqslant \varepsilon \leqslant 0.124$, a stress drop emerges in stress–strain curve (see figure 2(a)) implying the onset of plastic deformation of the composites. When a slight drop first comes up, it means the whole structure has just passed the yield point. This stress drop is attributed to the yield stage of Ni_3Al matrix as depicted in figure 3(b). The yield phenomenon originates from tensile deformation of some atoms in Ni_3Al matrix around the CNT, which can also be confirmed by a slight decrease in the stress–strain curves depicted in figure 4(a) between 5% and 10% strain [24, 25]. In addition, the white-color atoms in figure 3(b) are caused by temperature

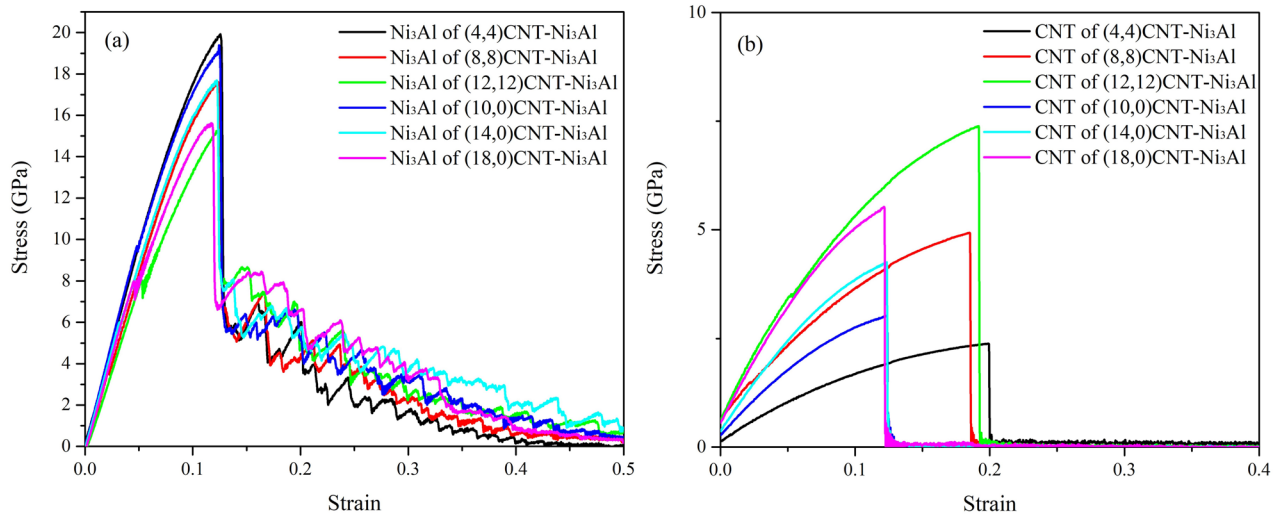

Figure 4. Stress contribution of individual component of reinforced composite: (a) Ni_3Al matrix, (b) CNTs to the total stress–strain behaviors of CNT-Ni_3Al composite under tension.

fluctuation through comparing with same simulation conducted under 1 K (see figure S4 in supporting information). Besides, the ultimate stresses all seem to be dependent on the defect induced by CNTs. Furthermore, as the tensile loading continues, the curve decreases dramatically when Ni_3Al matrix begins to fracture accompanied with the appearance of stacking faults captured by dislocation extraction algorithm (DXA) [50] in the $\{1,1,1\}$ slip bands (denoted as HCP phase) and void nucleation from the interface. Meanwhile, lattice disorder occurs around the void and lead to growth of the void to the surface. With the evolution of the deformation, void grows to form a crack at the surface of the composite and propagates quickly perpendicular to the loading direction until the overall fracture of Ni_3Al matrix though CNT still remained unbroken (figures 3(d)). The fracture behaviors of CNT-Ni_3Al composites are mainly governed by CNT strength where the CNT is just like a bridge connecting two fractured Ni_3Al parts postponing the overall fracture all the time. This phenomenon has also been discovered in experiments that some CNTs are observed linking the crack surfaces together, indicating a load transfer mechanism and a good interfacial bonding between the matrix and the reinforcement material (shear lag effect) [51]. Eventually, around the strain of 19%, another sharp decrease occurs in stress–strain curves due to the fracture of CNT as shown in figure 3(e). Meanwhile, regarding the case of zigzag CNT-reinforced composites, it is found that CNTs of all sizes break slightly earlier than final fracture of Ni_3Al matrix, which are around 12% strain (see table 1).

To better understand the strengthening mechanism of CNT-Ni_3Al composite, the overall stress–strain curves are separated into the contributions from Ni_3Al matrix and CNT, respectively, as is shown in figure 4. In figure 4(a), it is apparent to notice that the elastic modulus, yield stress, and fracture stress of Ni_3Al matrix decrease homogeneously with increasing radius of CNT due to the enlarging size of cylindrical hole in the centre. In figure 4(b), it is also clear to observe that the highest tensile stress is correlated with the largest radius of CNT both in armchair and zigzag CNT structures. However, either fracture stress or fracture strain provided by zigzag CNTs are much lower than those offered by armchair CNTs through comparing CNTs with different chiralities and similar radii. The main reason is that higher stress is needed for armchair CNT to transform into Stone–Wales defects [25]. Naturally, it can be concluded that inserted CNT makes strong contribution to improve the stiffness and strength of defected Ni_3Al matrix with enlarging radius owing to its large elastic modulus and fracture strain.

In case of CNT-Ni_3Al composites under compression, the evidence of plastic deformation occurs around $\varepsilon = -0.06$ when a little amount of atoms start to change into irregular forms marked in white color in the matrix, see figure 5(b). It can be observed from figures 5(b) and 6(b) that (8,8) CNT starts to buckle locally around $\varepsilon = -0.06$. Afterwards, Shockley partial dislocations form around the local buckled CNT and complex stacking faults appear on $\{1,1,1\}$ slip bands in Ni_3Al matrix conducted by DXA analysis [50]. As loading increases, more HCP phase strips develop and spread over the entire Ni_3Al matrix with CNT wrinkling more fierce (figure 5(c)) localized in its upper part until its limit at $\varepsilon = -0.25$. After that elastic reloading starts until $\varepsilon = -0.3$ with no new defects occur and even original defects would disappear with only two pseudo-twin boundaries left next to CNT, just as illustrated in figures 5(d) and (e). Here, the elastic reloading phenomenon is solely dependent on the Ni_3Al matrix rather than CNT impact since the pure one also manifests the same deformation form in figure 2(b). In this stage, multiple partial dislocations are nucleated within the pseudo-twin structure from the edges and the top surface. Shortly from $\varepsilon = -0.3$ on, additional Shockley partial dislocation is emitted, which leads continuous stress fluctuations with much more partial dislocations would nucleate from the pseudo-twin boundaries (see figure 5(f)).

Likewise, the contribution from CNT and Ni_3Al components are also analyzed during the compressive loading as shown in figure 6. Firstly, in figure 6(a), the overall tendency of stress–strain curves of Ni_3Al matrix decrease with

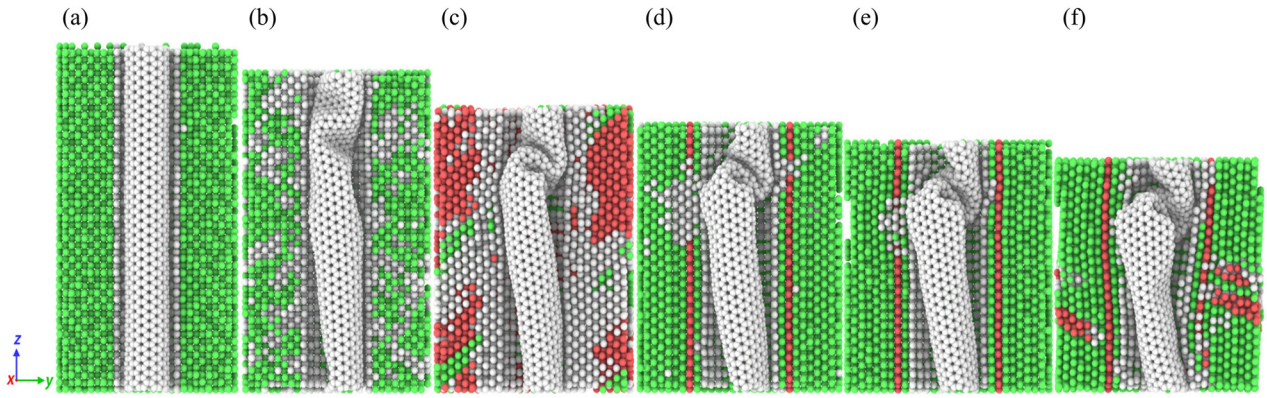

Figure 5. Snapshots of the different lattice structures of half-sliced (8,8) CNT-reinforced Ni_3Al at various strains: (a) −0.025, (b) −0.06, (c) −0.2, (d) −0.25, (e) −0.3, (f) −0.35.

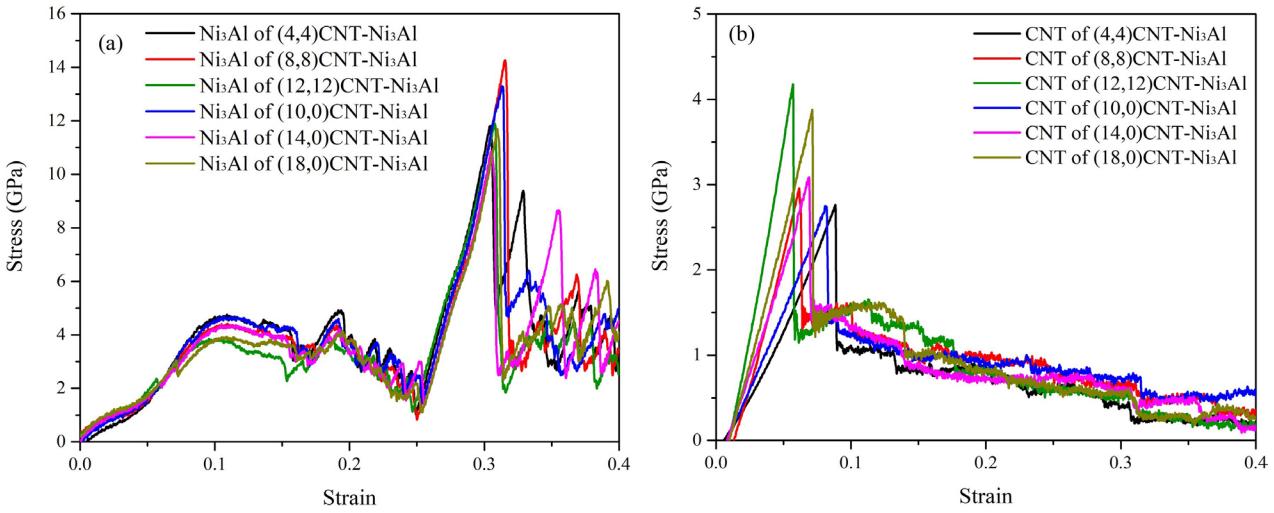

Figure 6. Stress contribution of individual component of reinforced composite: (a) Ni_3Al matrix, (b) CNTs to the total stress–strain behaviors of CNT-Ni_3Al composite under compression.

enlarging cylindrical centre hole, including elastic modulus and yield stress, which is similar with Amodeo's work [49]. Secondly in figure 6(b), it can be seen that elastic modulus increases with increasing CNT radii while yield strain shows the opposite trend (see table 2). As a consequence, the larger the CNT radius is, the more unstable the CNT will be, and start to buckle earlier. It also reveals that the CNT dominates the elastic zone of the whole composite by strengthening its stiffness. In other words, the inserted CNT brings excellent elastic properties to the composite while the Ni_3Al matrix provides considerable plasticity.

According to various stress–strain curves of CNT-Ni_3Al composite with different chiralities and radii, basic mechanical properties parameters, including Young's modulus, fracture stress, fracture strain under both tension and compression are given in tables 1 and 2. Here, it should be noticed that all fracture stresses are obtained when CNTs fracture. The tensile fracture stress increases steadily with increasing armchair CNT radius though they are still lower than pure Ni_3Al fracture stress and with a fluctuation. This indicates that the material itself could resist strong strength originally. Among them, the fracture stress of (8,8) demonstrates a drop to 8.71 GPa, which may be owing to slightly weaker elastic modulus of Ni_3Al matrix. The tensile fracture strain of the armchair CNT-reinforced composite remains around 19%, which is higher than that of the pure Ni_3Al (14%) and the zigzag CNT reinforcement (13%). From the discussion above it can be found that tensile fracture strain depends on the chirality of CNT rather than size, which is also the strain when CNTs fracture. In the mean time, through comparing the results of the two pairs of CNTs (6,6)-(12,0), (8,8)-(14,0), and (10,10)-(16,0) with almost the same parameters and volume fractions, most mechanical properties of the zigzag CNT-reinforced composites are superior to armchair ones except the fracture strain, indicating that the zigzag CNT-reinforced composite can better be accustomed to tensile condition than the armchair CNT-reinforced composites since zigzag CNTs are much stiffer (see table 3). On the other hand, both compressive yield stress and strain decline with increasing size (see table 2) since premature failure of the CNT-Ni_3Al originates from local buckling of CNT. However, it seems that there is a transition point in yield stress between (10,10) and (12,12) CNT's, as well as (16,0) and (18,0). From figure 6(b), it can be found a drastic increase (about 1 GPa) of CNT yield stress for both armchair and zigzag CNT types at this transition point. Meanwhile, we further simulate the (16,16) and (20,20)

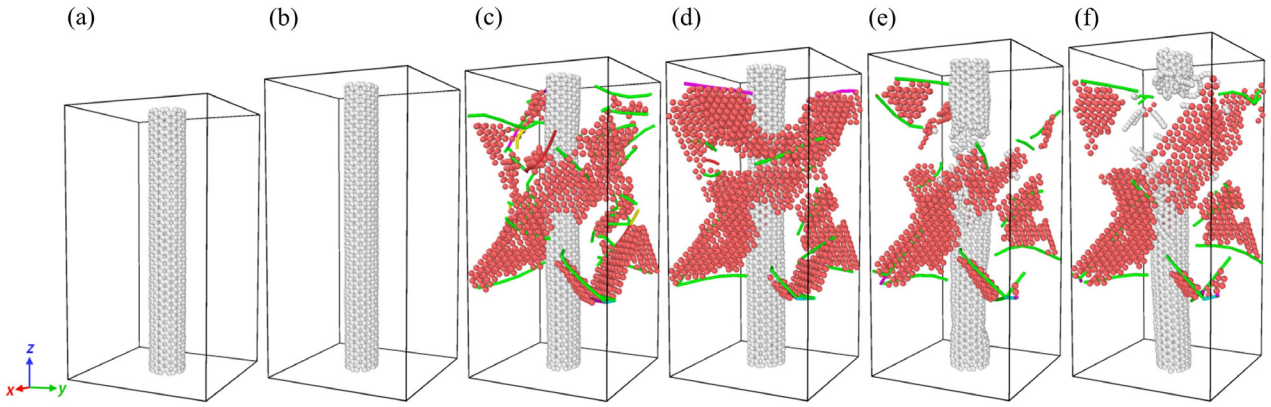

Figure 7. Dislocation and defect evolution with rising strain of CNT-Ni_3Al composite at various strains: (a) 0.01, (b) 0.1, (c) 0.13, (d) 0.16, (e) 0.185 75, (f) 0.21. Red atoms represent HCP phase between dislocations. The green curves represent Shockley dislocations.

CNT-reinforced composites under compression. The yield stresses are −7.18 GPa and −8.28 GPa, respectively. The yield stress transition at particular point would mostly be contributed by the transition point of yield stress of inserted CNT at certain radius. According to Wang's work [52], it is concluded that the critical buckling force drops with increasing aspect ratio (*L*/*D*, *L* stands for CNT length, *D* stands for CNT diameter) for single-wall CNTs. Therefore, in our work the steadily decreasing aspect ratio *L*/*D* with larger CNTs is bound to cause the tendency transition in yield stress.

The elastic modulus of aligned CNT reinforced composites at micro-scale can be estimated using the well-established rule of mixtures (ROM) [22]. The elasticity is calculated by

$$Y_{\text{CNT-Ni}_3\text{Al}} = Y_{\text{CNT}}V_{\text{CNT}} + Y_{\text{Ni}_3\text{Al}}V_{\text{Ni}_3\text{Al}}, \tag{5}$$

$$V_{\text{CNT}} = \frac{2\pi rhl}{V - \pi(r+3)^2 l}, \tag{6}$$

$$Y_{\text{CNT}} = \frac{Y'_{\text{CNT}}V}{2\pi rhl}, \tag{7}$$

where $Y_{\text{CNT-Ni}_3\text{Al}}$ is the Young's modulus of CNT reinforced Ni_3Al composite. Y_{CNT} (also calculate the slope ratios of stress–strain curves around zero $0 \leqslant \varepsilon \leqslant 0.01$) and $Y_{\text{Ni}_3\text{Al}}$ are the Young's moduli of the CNT and Ni_3Al among the composites, respectively. V_{CNT} and $V_{\text{Ni}_3\text{Al}}$ are the volume fractions of the CNT and Ni_3Al, respectively. The thickness *h* is chosen as 3.4 Å in consistence with the interlayer space of graphite and 3 Å in equation (6) means extra distance between CNT and Ni_3Al in the model, *V* is the volume of simulation box, *r* is the radius of a CNT, and *l* is the length of a CNT. Y'_{CNT} is denoted as the elastic modulus calculated from figure 4. The calculated elastic moduli are summarized in table 3 and it can be noticed that the calculated values presented in table 3 are in good agreement with present MD simulation results though theoretical results are slightly lower than simulation results. The main reason for this discrepancy may originate from slightly lower $Y_{\text{Ni}_3\text{Al}}$, which is calculated through dividing the simulation box volume. Nevertheless, it is demonstrated that minor CNT fraction (ranging from 1% to 8% in this study) could provide adequate strengthening effect with dropping values of $Y_{\text{Ni}_3\text{Al}}$ and this mixture rule can be an effective method to predict the elasticity of CNT composites with Ni_3Al matrices.

3.2. Dislocation and structure analysis

In this article, the analysis of dislocations and void defects are conducted through the DXA analysis contained in software OVITO [50, 53]. Figure 7 presents the dislocation evolution of CNT-reinforced Ni_3Al composite under tensile loading at some typical strains. It is shown that the unit cell is stretched from the very beginning, Ni_3Al matrix dominates the elastic region as Young's modulus of CNT is much larger than that of Ni_3Al. Hence, the Ni_3Al matrix always yield firstly. When both components are subjected to the same tensile force, the corresponding strains vary hugely, causing the appearance of relative interfacial displacement and interfacial shear stress to delay the elastic deformation to a certain extent in Ni_3Al phase. This is also the reason why declining elastic modulus of Ni_3Al matrix is improved by embedded CNT (see table 3). When the stress in the unit cell increases beyond the yield stress of Ni_3Al matrix, extra energy brought by external force could not be absorbed by the elastic deformation. Then the stress or energy is released by producing massive amount of dislocation structures in Ni_3Al matrix, as shown in figures 7(c) and (d). However, the inserted CNT plays a critical role in hindering the mobility, motion of dislocation and slip bands derived from Ni_3Al matrix. To explain this probable explanation evidence, the HCP phase atoms fraction is focused on to track the dislocation development directly. As shown in figure 8, throughout the strains under tension beyond 15%, it can be seen that the HCP atoms fraction remains the same (9%) for pure Ni_3Al model. For the rest various CNT-reinforced composites, their evolutionary values of HCP phase fraction cannot surpass the pure Ni_3Al model reference's, indicating that CNT indeed plays a role in inhibiting dislocation development and its density in the matrix. In addition, all composites deform around 10% strain slightly earlier than pure Ni_3Al model (13%) due to broken structure integrity.

On the other hand, it can be observed that a bunch of Shockley partial dislocations loop appear around the CNT along the tensile direction as shown in figures 7(c) and (d), acting as forests of dislocations. Generally, pair of green partial dislocations may lead to the appearance of stacking fault ribbon between them as dislocation slip owing to rather higher stacking fault energy (SFE: 0.3 J m^{-2}). These dislocations form Orowan looping and further restrict or hamper the movement of newly born dislocations and vacancies near

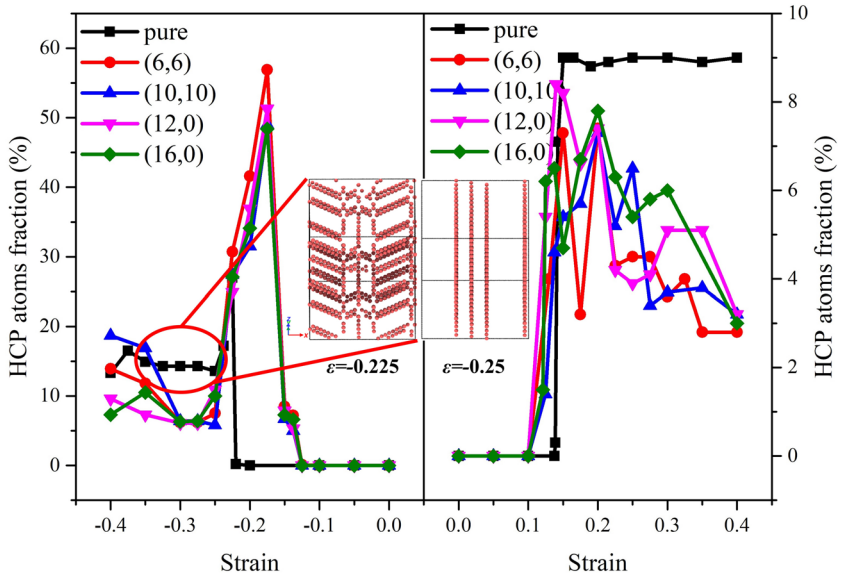

Figure 8. HCP phase atoms fraction changes as a function of strain under tension and compression for CNT-Ni_3Al composites and pure Ni_3Al. The insets show the pseudo-twin structures (HCP phase) evolution in the pure Ni_3Al phase.

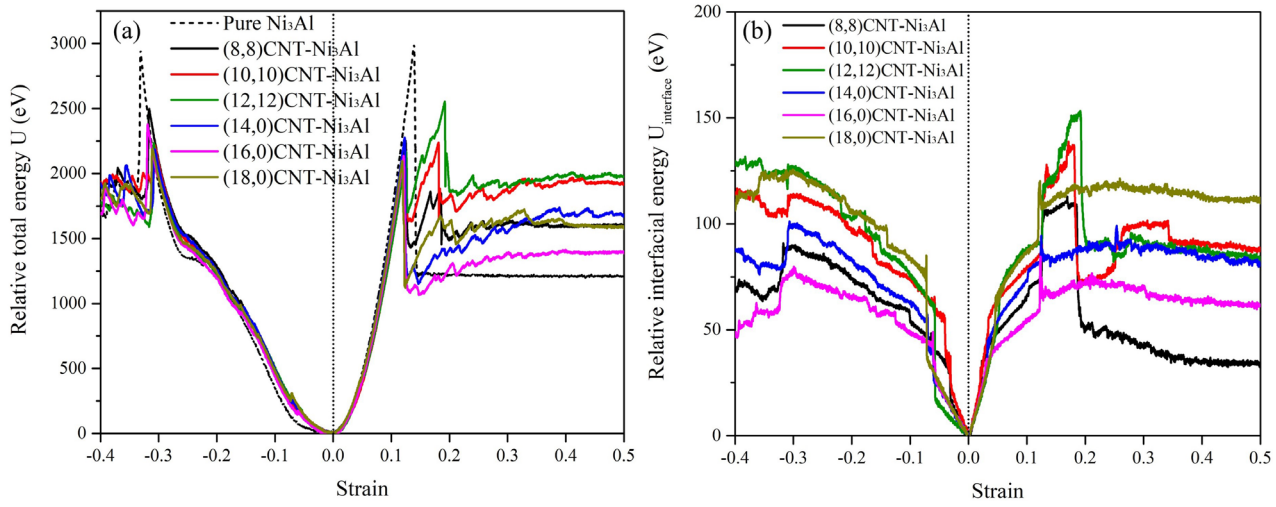

Figure 9. The calculated (a) relative total energy and (b) relative interfacial vdWs energy of CNT-Ni_3Al composite changes as a function of strain under both tension and compression.

the CNT to overcome the interface [25]. This phenomenon is called 'Orowan strengthening effects'. Thus, to introduce more dislocations, higher stress is needed in the composite. As a consequence, once higher stress is beyond the ultimate stress of the whole structure, voids will change into cracks in the internal structure with density of dislocations will gradually decrease, as illustrated in figures 7(d)–(f), and 8. This is the another reason for the aforementioned strengthening effect.

Meanwhile, the interfacial shear stress continues to block the stretching of Ni_3Al matrix in order to maintain compatible deformation between CNT and Ni_3Al matrix. Figure 9 shows the relative total energies and relative interfacial van der Waals (vdWs) energies changing as functions of tensile and compressive strains [22], which are attained through subtracting the initial energy for CNT-Ni_3Al itself and the interface. To minimize the size effect for better analysis, we choose similar sizes with different chiralities (for instance (8,8)-(14,0) and (10,10)-(16,0)) to focus solely on chirality effect. For $0 \leqslant \varepsilon \leqslant 0.1$, all curves turn out to be similar in spite of tiny differences, indicating that the elastic behavior of the CNT-Ni_3Al composite is mostly governed by their individual contributions, but has little business with interface. It can be found in table 1 that Young's moduli of zigzag CNT-reinforced composites are higher than those of armchair CNT-reinforced models when the sizes of CNTs are similar since zigzag CNTs are much stiffer. For $\varepsilon > 0.1$, it is clearly seen that armchair CNT-reinforced structures have more interfacial energies rises compared with zigzag ones, meaning that more displacements happen along Ni, Al atoms and CNTs in former cases than in latter cases, especially when strain is between 12% and 20%. During this stage, it can be seen there are similar growths in both total energy and interfacial energy, and the interfacial energy rise is around 60 eV for (12,12)CNT-Ni_3Al, which is around 8% of the total energy increase.

Figure 10 illustrates the dislocation evolution of CNT-Ni_3Al composite under compression. It is clearly observed

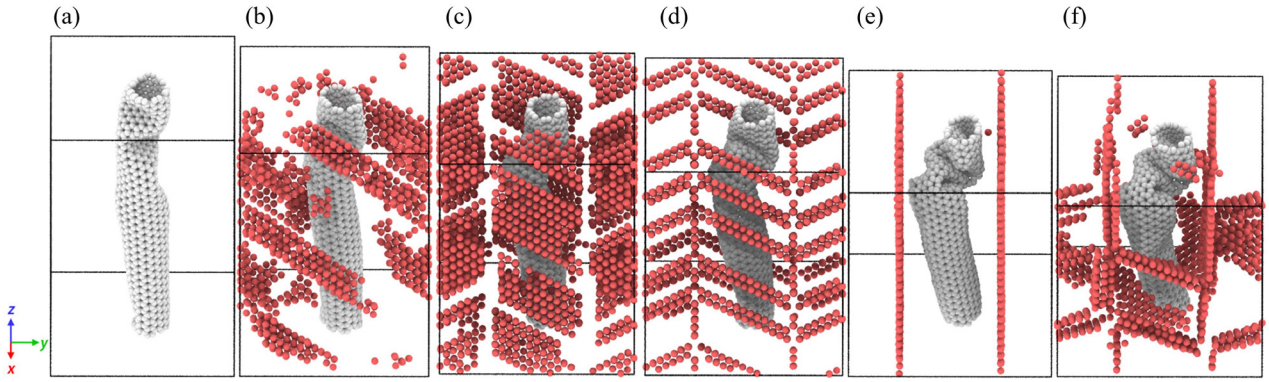

Figure 10. Dislocation evolution of CNT-Ni_3Al composite under compression with various strains: (a) −0.1, (b) −0.15, (c) −0.2, (d) −0.225, (e) −0.3, (f) −0.35.

that most dislocations are produced surrounding the inserted CNT (see figure 10(b)) surrounding the locally buckled CNT until occupying the whole matrix. Afterwards, from figures 10(c) and (d) it can be found that pseudo-twin structure appears with ongoing compression and large amounts of partial dislocations transform into pseudo-twin FCC structure with only two pseudo-twin boundaries left before the reloading process. Slip transformation takes place on the symmetrical planes and it can be seen that large slip steps are produced by the subsequent slip of multiple dislocations on the same slip plane. And after the reloading process, newly born HCP phase slips bands are emitted between two twin boundaries. Compared with pure Ni_3Al compression in figure 8, the produced HCP fraction is two times more than pure one's, implying that inserted CNT cannot realize reducing dislocation density just as the results under tension. Besides, we also find that the twin boundaries are doubled in pure Ni_3Al (see figure 8), which make dislocations development more difficult. Twin boundaries reduction can as well explain why HCP fraction goes up for most cases after 30% strain. Through contrasting figure 9(a) and (b), it is found that interfacial energy increase under compression is incomparable to that of the total energy. Therefore, the CNT insertion can only provide strengthen effect during elastic stage and the plastic stage is mainly dependent on Ni_3Al matrix. Moreover, the higher HCP atoms fraction under compression can be explained from the view of total energy change where the total energy increase in compression mode during 12% and 25% strain is lower than that under tension. It should be known that plastic deformation always leads to lower energy. So the formation of dislocation and twins is apparently effective under compression, causing much more slip bands.

4. Discussion

4.1. CNT volume fraction influence

Referring from results of components analysis and figure 4, it can confirm that the optimization in mechanical properties is mainly owing to inserted CNTs. However, from the aforementioned simulation results, it can be directly seen from figure 4 that it is difficult to evaluate the contribution of the CNT reinforcement to the overall enhancement of mechanical properties since the contribution of the matrix decreases and that of the CNT increases as the size of CNT increases. Therefore, the effect of the matrix should be kept same to analyze the effect of the CNT reinforcement. However, keeping the highest volume of Ni_3Al matrix would lead to larger gap between smaller size CNTs and Ni_3Al (The larger gap here means the gap between CNT and inside face of Ni_3Al matrix rather than the gap between CNT and the other one from periodic models.), and this situation would probably weaken the contribution from the interfacial part. So it would be inappropriate to discuss the solely influence from CNT while keeping the volume of Ni_3Al phase all the same. As a matter of fact, on the other hand we could find that the different models of CNT-Ni_3Al vary with both CNT sizes and CNT volume fraction since CNT volume fraction is a focus in experimental studies. Specifically, changing the volume of Ni_3Al phase would not change the influence of interface strength. So, in order to clarify effects of CNT sizes and CNT volume fractions, one factor is kept constant to investigate another factor's effect, separately. Then, we carry out the study of the (4,4), (6,6), (8,8), (10,10) CNTs and 1%–5% CNT volume fractions with enlarging Ni_3Al phase calculated from equation (6) in order to maintain the constant volume fractions.

Taking (6,6)CNT as an example for CNT size factor and 4% for CNT volume fraction effect, figure 11 gives stress–strain curves of the overall configurations and the CNT components, including volume fractions vary from 1% to 5% and CNT sizes range from (4,4) to (10,10). An opposite strengthening trend is observed through comparing figures 11(a) and (b) concerning size effect and volume fraction effect. In figure 11(a), the improvement of mechanical properties can be seen with the increasing CNT volume fraction. In contrast, the overall mechanical behaviors decline with increasing CNT size. On the other hand, comparing the stress contribution from CNTs in figures 11(a) and (b), a critical variation is observed for the different volume fractions, while no variation is observed for the different sizes. To be concluded, the CNT volume fractions a more significant role in strengthening the whole structures than CNT size effect, and the conclusion is similar with previous work studying BNNT-Al composites [32]. So in engineering applications, it is suggested that higher

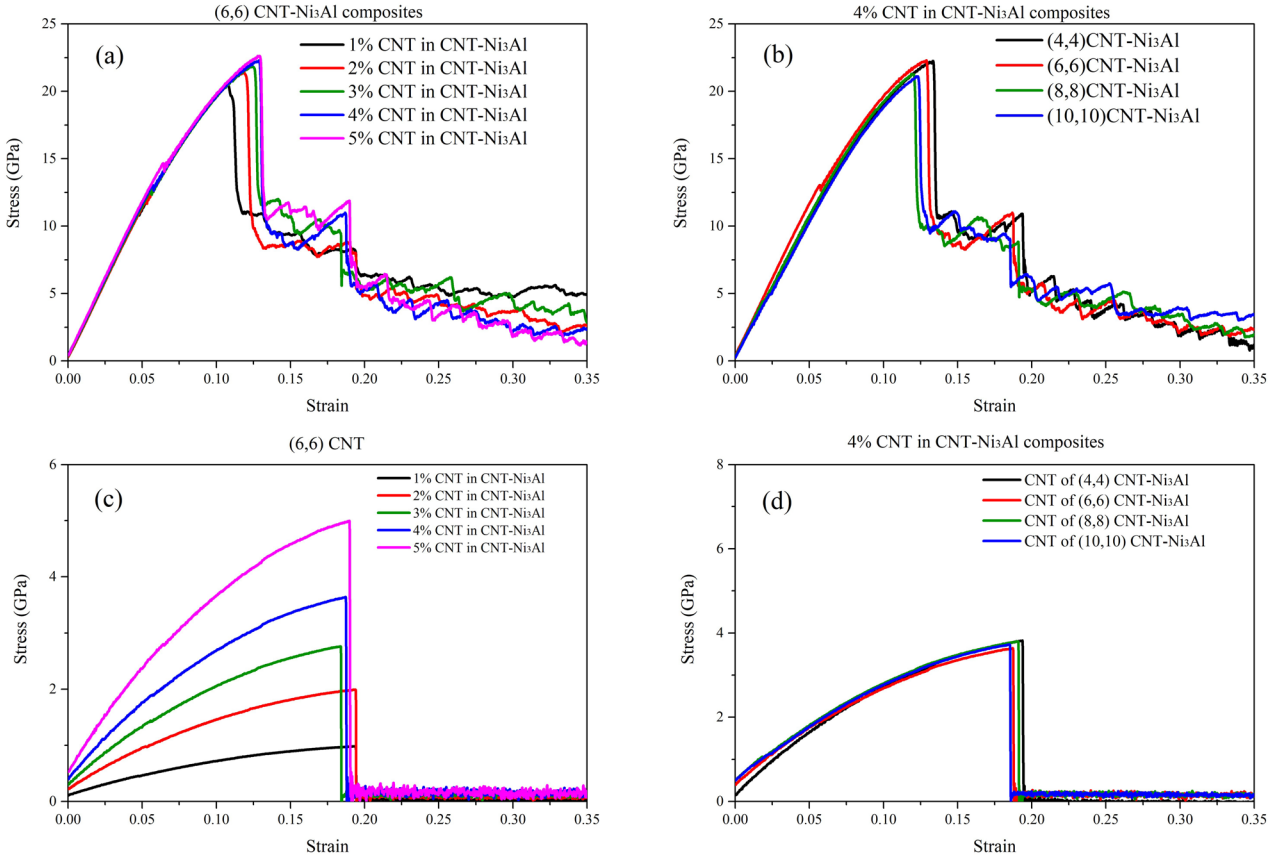

Figure 11. Effect of the volume fraction and size of CNTs on the stress–strain response: (a) stress–strain curves of the (6,6)CNT-Ni_3Al composites with the volume fraction ranging from 1% to 5%, (b) stress–strain curves of the CNT-Ni_3Al composites with the same volume fraction of 4% and with different sizes of CNTs, (c) stress contribution of the CNT components in (6,6)CNT-Ni_3Al composites, and (d) stress contribution of the 4% CNT component in CNT-Ni_3Al composites with various sizes of CNTs.

CNT volume fraction with smaller size effect should be better than solely adding large size CNTs.

With regard to experimental studies, many papers have focused on the improvement of mechanical behaviors brought by increasing CNT volume fractions. After all, the size of CNTs could not be controlled precisely so the volume fraction is concerned widely. Soon H. Hong's group found that both the yield strength and Young's modulus were increased by increasing the CNTs volume fraction in CNT/Cu nanocomposites [54]. Some other groups also find the same increasing trend with elastic modulus and yield strength in multi-wall CNT/Cu and CNT/Al nanocomposites [55, 56]. In the present study, we also do some statistics on elastic modulus and yield strength changing with CNT volume fractions for all cases, as shown in figure 12. The elastic modulus in figure 12(a) shows two different tendencies. Only (4,4)CNT-Ni_3Al composites behave abnormally showing declining trend with enlarging CNT volume fraction. We further calculate the overall Young's moduli of (4,4), (6,6), (8,8), and (10,10) CNT-Ni_3Al composites with different CNT volume fractions according to the rule of mixtures (ROM). The results are concluded in table S3 in supporting information. It should be noticed that the main reason for decrease of Young's modulus for (4,4) CNT-Ni_3Al composites is the prominent decrease of Y_{Ni_3Al} compared with other 3 groups. Meanwhile, the statistics are in a good agreement with the tendency of MD simulations. The rest three CNT sizes all behave linearly with enlarging CNT volume fraction and also the increments are almost the same (10 GPa) for a single CNT size when the fraction changes from 1% to 5%. It is also interesting to notice that the (6,6)CNT-Ni_3Al composites have the highest elasticities among all cases, which is consistent with tendency in tables 1 and 3. On the other side, the statistics of yield strength are shown in figure 12(b) where for all occasions the yield strength increases linearly with CNT volume fractions from 1% to 5%. Furthermore, yield strengths of (4,4) and (6,6)CNT-Ni_3Al composites are slightly higher than the other two configurations with approximately 1 GPa. Basically, from the results of elasticities and yield strength in figure 10 are in good agreement with previous related experimental researches.

4.2. Temperature influence

On account of high temperature resistance of Ni_3Al matrix, it is necessary to pay attention to temperature effect on its overall property. In the present work, a temperature gradient of 300 K, 600 K, 900 K, and 1200 K is considered in the simulations. Some basic parameters have been collected in figure 13. It is shown in figure 13 that elastic modulus of the composite under tension decreases slightly from 225.46 GPa to 174.75 GPa, indicating that high temperature destroys the whole structure to some extend [57]. On the other hand, under

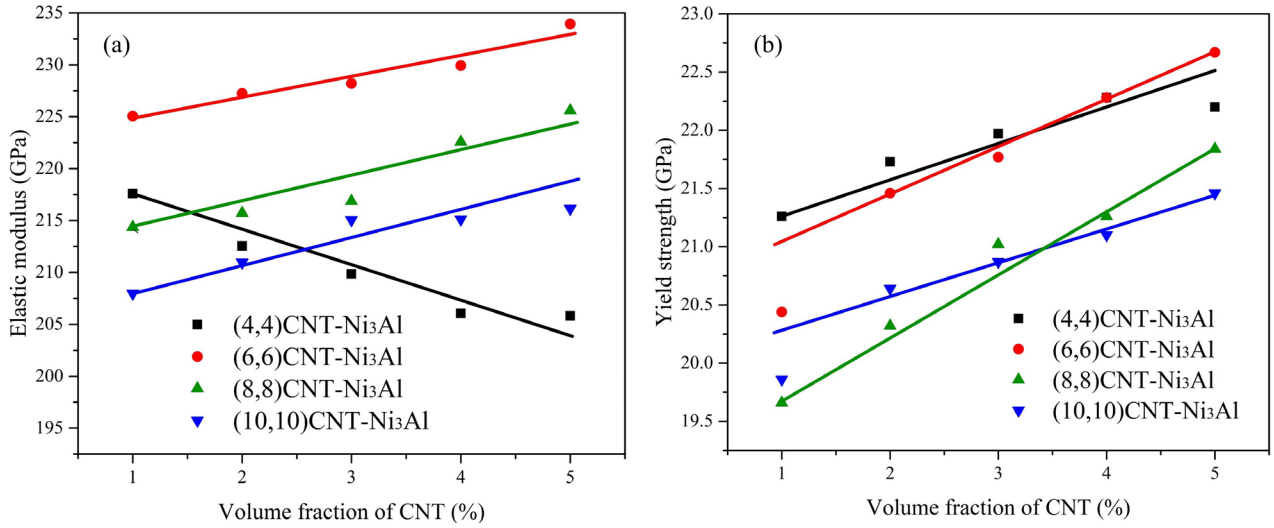

Figure 12. Calculated (a) elastic moduli and (b) yield strengths of CNT-Ni_3Al composites with different volume fractions and sizes of CNTs.

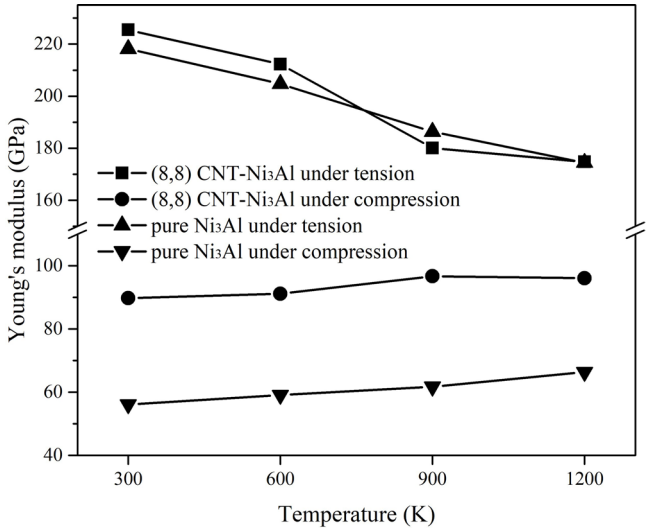

Figure 13. Young's modulus of both pure Ni_3Al and (8,8)CNT-Ni_3Al composite under tension and compression with different temperatures.

compression the Young's modulus stays around a fixed value (90 GPa). At mean time, pure Ni_3Al model is tested under the same conditions and results are shown in figure 13. It can be found that similar trends also happen on pure Ni_3Al model. Young's modulus of pure Ni_3Al under tension drops from 218.17 GPa to 174.43 GPa while it keeps around 60 GPa under compression. The overall mechanical property could be stable with increasing temperature, which indicates that the material itself has a good stability under compression with higher temperatures. A massive advancement of elastic property can also be judged under compression through comparing elastic modulus of both pure Ni_3Al and CNT-Ni_3Al composites. Even under tension, CNT is not the reason for weakening of elastic modulus. Therefore, the inserted CNT indeed plays a positive role in stabilizing the elastic performance of the CNT-Ni_3Al composites under higher temperature, which is preferred in practical applications but has not been focused previously. The present results could provide a beneficial reference for future experiments and engineering applications.

5. Conclusions

In summary, extensive MD simulations are conducted to investigate the mechanical behavior of CNT-Ni_3Al composites under tension and compression. Especially, The role of chirality, temperature, and volume fraction of CNT on the mechanical properties of the highly aligned CNT-Ni_3Al composites are ayalyzed and discussed in details. The main conclusions of this study are listed as follows:

(1) The dispersion of a minor fraction of a CNT into Ni_3Al matrix leads to a sufficient enhancement in the stiffness of CNT-Ni_3Al composites compared with pure Ni_3Al. The tensile fracture stress relies on CNT sizes while tensile fracture strain depends on CNT chiralities. Zigzag CNTs can provide more strength for raising elastic modulus while armchair CNTs can provide superior elongation. The measured elasticities of CNT/Ni_3Al composites are reasonably agreed with estimated values, basing on the rule of mixture. Under compression, CNTs only work in the elastic stage.

(2) The deformation regime is mainly governed by CNT strength under tension while under compression it mainly relies on Ni_3Al matrix. CNT plays a critical role in hindering further dislocation propagation and ultimate fracture under tension. Robust interfacial interactions are assurance for CNT strengthening effect. However, the situation is opposite under compression. Through comparing the changing amplitudes of relative interfacial energy and numbers of pseudo-twin boundaries with pure Ni_3Al, it can be confirmed that slip bands formation during compression is more effective than that under tension in the same mode.

(3) Well-designed quantitative simulations imply that increasing volume fraction is a direct and effective

method to enhance the overall mechanical properties both in elasticities and yield strengths rather than raising CNT sizes merely. At last, gradient temperatures are set to calculate the mechanical reactions, and it is found that CNT could be a potential reinforcement material under higher temperature.

The present work offers a theoretical framework for predicting the mechanical properties of CNT-reinforced composites from the micro-scale models. This work can be spread to investigate mechanical behaviors of other types of nanotubes reinforced composites and shed some light on the design of CNT-reinforced composites in nanoscale engineering.

Acknowledgment

This work is supported by the National Natural Science Foundation (Grant No 11872309) of China and the Fundamental Research Funds for the Central Universities (Grant No. 3102017JC01003) of China.

ORCID iDs

Zhaowei Wang https://orcid.org/0000-0002-9853-6043
Liangzhi Kou https://orcid.org/0000-0002-3978-117X
Chun Li https://orcid.org/0000-0002-0901-0294

References

[1] Li Y, Zhao H, Zeng G, Guan C and He X 2004 *Mater. Lett.* **58** 1629–33
[2] Pollock T and Tin S 2006 *J. Propul. Power* **22** 361–74
[3] Socrate S and Parks D 1993 *Acta Metall. Mater.* **41** 2185–209
[4] Hazotte A, Bellet D, Ganghoffer J, Denis S, Bastie P and Simon A 1992 *Phil. Mag. Lett.* **66** 189–96
[5] Iijima S 1991 *Nature* **354** 56–8
[6] Salvetat J, Bonard J, Thomson N, Kulik A, Forro L, Benoit W and Zuppiroli L 1999 *Appl. Phys.* A **69** 255–60
[7] Ruoff R and Lorents D 1995 *Carbon* **33** 925–30
[8] Sharma S, Chandra R, Kumar P and Kumar N 2014 *Comput. Mater. Sci.* **86** 1–8
[9] Yang S, Choi J and Cho M 2015 *Compos. Struct.* **127** 108–19
[10] Mahboob M and Islam M Z 2013 *Comput. Mater. Sci.* **79** 223–9
[11] Neubauer E, Kitzmantel M, Hulman M and Angerer P 2010 *Compos. Sci. Technol.* **70** 2228–36
[12] Bakshi S R, Lahiri D and Agarwal A 2010 *Int. Mater. Rev.* **55** 41–64
[13] Dong S, Zhu C, Chen Y and Zhao J 2019 *Carbon* **141** 348–62
[14] Jiang L, Li Z, Fan G, Cao L and Zhang D 2012 *Carbon* **50** 1993–8
[15] Chen C L and Lin C H 2015 *Metall. Trans.* A **46A** 3687–95
[16] Housaer F, Beclin F, Touzin M, Tingaud D, Legris A and Addad A 2015 *Mater. Charact.* **110** 94–101
[17] Jagannatham M, Sankaran S and Haridoss P 2015 *Mater. Sci. Eng.* A **638** 197–207
[18] Chen Y, Lu F, Zhang K, Nie P, Hosseini S R E, Feng K and Li Z 2016 *Carbon* **107** 361–70
[19] Wu Y, Kim G Y and Russell A M 2012 *Mater. Sci. Eng.* A **538** 164–72
[20] Simoes S, Viana F, Reis M A L and Vieira M F 2014 *Compos. Struct.* **108** 992–1000
[21] Song H Y and Zha X W 2010 *Comput. Mater. Sci.* **49** 899–903
[22] Silvestre N, Faria B and Lopes J N C 2014 *Compos. Sci. Technol.* **90** 16–24
[23] Zhou X, Song S, Li L and Zhang R 2016 *J. Compos. Mater.* **50** 191–200
[24] Choi B K, Yoon G H and Lee S 2016 *Composites* B **91** 119–25
[25] Xiang J, Xie L, Meguid S A, Pang S, Yi J, Zhang Y and Liang R 2017 *Comput. Mater. Sci.* **128** 359–72
[26] Li C, Shang J, Kou L and Yue Z 2015 *Aip Adv.* **5** 077136
[27] Shang J, Yang F, Li C, Wei N and Tan X 2018 *Comput. Mater. Sci.* **148** 200–6
[28] Ji L, Ouyang M and Sun D 2017 *Chem. Eng. Equip.* **2** 24–6 (in Chinese)
[29] Rao P, Suryanarayana S, Murthy K and Naidu S 1989 *J. Phys.: Condens. Matter* **1** 5357–61
[30] Wang L, Cai C, Zhou Y and Zhou G 2017 *J. Phys. Chem.* C **121** 19191–200
[31] Faria B, Guarda C, Silvestre N, Lopes J N C and Galhofo D 2018 *Composites* B **145** 108–20
[32] Cong Z and Lee S 2018 *Compos. Struct.* **194** 80–6
[33] Plimpton S 1995 *J. Comput. Phys.* **117** 1–19
[34] Pun G P P and Mishin Y 2009 *Phil. Mag.* **89** 3245–67
[35] Stuart S, Tutein A and Harrison J 2000 *J. Chem. Phys.* **112** 6472–86
[36] Huang S-P, Daniela S M and Balbuena P B 2003 *Sur. Sci.* **545** 163–79
[37] Muller S E, Santhapuram R R and Nair A K 2018 *Comput. Mater. Sci.* **152** 341–50
[38] Shibuta Y and Maruyama S 2007 *Comput. Mater. Sci.* **39** 842–8
[39] Xia Z, Liu X, Sansoz F and Shen M 2018 *Appl. Phys.* A **124** 506
[40] Ke D, Li L, Hu Y and Wang X 2017 *Mater. Des.* **133** 455–63
[41] Verkhovtsev A V, Schramm S and Solov'Yov A V 2014 *Eur. Phys. J.* D **68** 1–11
[42] Katin K P, Prudkovskiy V S and Maslov M M 2018 *Micro Nano Lett.* **13** 160–4
[43] Prikhodko S V, Yang H, Ardell A J, Carnes J D and Isaak D G 1999 *Metall. Mater. Trans.* A **30** 2403–8
[44] Hua H, Wen Z, Zhao Y, Li F, Nan W and Han P 2014 *Intermetallics* **44** 110–5
[45] Yang X and Hu W 2014 *J. Appl. Phys.* **115** 113507
[46] Bing J, Liu C, Zhang C, Liang R and Wang B 2009 *Composites* B **40** 212–7
[47] Kundalwal S and Ray M 2011 *Int. J. Mech. Mater. Des.* **7** 149–66
[48] Kundalwal S and Ray M 2014 *Mech. Mater.* **53** 47–60
[49] Amodeo J, Begau C and Bitzek E 2014 *Mater. Res. Lett.* **2** 140–5
[50] Stukowski A, Bulatov V V and Arsenlis A 2012 *Modelling Simul. Mater. Sci. Eng.* **20** 085007
[51] Bradbury C R, Gomon J K, Kollo L, Kwon H and Leparoux M 2014 *J. Alloys Compd.* **585** 362–7
[52] Wang C M, Roy Chowdhury A N, Koh S J A and Zhang Y Y 2014 *Modeling of Carbon Nanotubes, Graphene and their Composites* (Berlin: Springer) pp 239–73
[53] Stukowski A 2010 *Modelling Simul. Mater. Sci. Eng.* **18** 015012
[54] Daoush W M, Lim B K, Mo C B, Dong H N and Hong S H 2009 *Mater. Sci. Eng.* A **513** 247–53
[55] Kim K T, Cha S I, Hong S H and Hong S H 2006 *Mater. Sci. Eng.* A **430** 27–33
[56] Esawi A M K, Morsi K, Sayed A, Taher M and Lanka S 2010 *Compos. Sci. Technol.* **70** 2237–41
[57] Yu J, Zhang Q and Yue Z 2014 *RSC Adv.* **4** 20789–96